Solar Physics (2006) 236: 325–349
DOI: 10.1007/s11207-006-0039-z

ANALYSIS OF MAGNETIC SHEAR IN AN X17 SOLAR FLARE ON OCTOBER 28, 2003

Y.N. SU
Harvard-Smithsonian Center for Astrophysics, Cambridge, MA 02138, U.S.A.; Purple Mountain Observatory, Chinese Academy of Sciences, Nanjing 210008, P. R. China; Graduate University of Chinese Academy of Sciences, Beijing, P. R. China
(e-mail: ynsu@head.cfa.harvard.edu)

L. GOLUB and A.A. VAN BALLEGOOIJEN
Harvard-Smithsonian Center for Astrophysics, Cambridge, MA 02138, U.S.A.

and

M. GROS
DSM/DAPNIA/Service d'Astrophysique, CEA Saclay, 91191 Gif-sur-Yvette, France

(Received 1 August 2005; accepted 9 May 2006)

Abstract. An X17 class (GOES soft X-ray) two-ribbon solar flare on October 28, 2003 is analyzed in order to determine the relationship between the timing of the impulsive phase of the flare and the magnetic shear change in the flaring region. EUV observations made by the *Transition Region and Coronal Explorer* (TRACE) show a clear decrease in the shear of the flare footpoints during the flare. The shear change stopped in the middle of the impulsive phase. The observations are interpreted in terms of the splitting of the sheared envelope field of the greatly sheared core rope during the early phase of the flare. We have also investigated the temporal correlation between the EUV emission from the brightenings observed by TRACE and the hard X-ray (HXR) emission ($E > 150$ keV) observed by the anticoincidence system (ACS) of the spectrometer SPI on board the ESA INTEGRAL satellite. The correlation between these two emissions is very good, and the HXR sources (RHESSI) late in the flare are located within the two EUV ribbons. These observations are favorable to the explanation that the EUV brightenings mainly result from direct bombardment of the atmosphere by the energetic particles accelerated at the reconnection site, as does the HXR emission. However, if there is a high temperature ($T > 20$ MK) HXR source close to the loop top, a contribution of thermal conduction to the EUV brightenings cannot be ruled out.

1. Introduction

A two-ribbon structure in the chromosphere and transition region (e.g., in Hα, UV, and EUV) is often seen during a solar flare, especially for those long-duration events associated with coronal mass ejections (CMEs). The magnetic reconnection model proposed by Carmichael (1964), Sturrock (1966), Hirayama (1974), and Kopp and Pneuman (1976) (the CSHKP model) suggests that for an eruptive flare or CME, field lines open and then merge and reconnect at progressively higher altitudes in the corona. The EUV ribbons are the footprints in the transition region of the

closed, reconnected field lines which are typically filled with hot coronal plasma in the form of postflare loops.

There are two proposed mechanisms for producing the EUV ribbon emission: thermal conduction from the reconnected loops, and direct bombardment of the lower atmosphere by accelerated particles from the reconnection site (Fletcher and Hudson, 2001). A close temporal relationship between the hard X-ray (HXR) and UV emission during the impulsive phase in solar flares was reported by Kane and Donnelly (1971) and Kane, Frost, and Donnelly (1979) using data from OGO and OSO satellites and was also found by SMM, when HXR and UV light curves were seen to be simultaneous to within 1 s (Woodgate *et al.*, 1983; for a review, see Fletcher, 2002).

Cheng *et al.* (1981) and Cheng, Tandberg-Hanssen, and Orwig (1984) made the first attempt to study the spatial structure of UV bursts using the UV observations with spatial resolution of a few seconds of arc obtained by UVSP. Their study showed that: (a) there was considerable preflare activity with UV transient brightenings occurring in many small point-like kernels; and (b) individual peaks in the HXR bursts can be identified with individual peaks in the UV bursts of individual flaring kernels. The recent observations from *Transition Region and Coronal Explorer* (TRACE), *Yohkoh*, and BATSE reported by Warren and Warshall (2001) showed that the initial HXR burst was positively correlated only with footpoints that showed no pre-HXR activity, which indicated that energy release during the preflare and impulsive phase of the flare was occurring on different loops. A comparison of HXR emission and EUV emission measured at the locations of the HXR sources was reported by Fletcher and Hudson (2001), who found that the light curves map to one another quite well. However, due to the TRACE time resolution of the event they reported, they could only establish that the two peaks are within 20 s of each other.

It is well known that during a two-ribbon flare the two footpoint ribbons, residing in opposite magnetic polarities, expand outward and away from each other (Svestka and Cliver, 1992). Some recent papers even reported an anticorrelation between the time profile of the separation distance of the conjugate footpoints and that of the HXR emission in a flare on September 9, 2002 (Ji *et al.*, 2004a,b; Huang and Ji, 2005). In addition to the ribbon separation in the direction perpendicular to the magnetic inversion line (MIL), which is predicted generically by the two-dimensional magnetic reconnection model, motions of the footpoints parallel to the direction of the MIL during flares have also been found by several authors. Masuda, Kosugi, and Hudson (2001) reported observations of the evolution of the HXR (*Yohkoh*/HXT) footpoints from a strong to a weak sheared structure, which was also found in Hα (Sartorius Refractor at Kwasan Observatory; Asai *et al.*, 2003) observations. A shear change of the footpoints observed at HXR (RHESSI) and microwave (Nobeyama Radioheliograph) was also reported by Kundu, Schmahl, and Garaimov (2004). This strong-to-weak shear change of the footpoints reflects a decrease in the shear of the newly reconnected loops during the course of the flare.

It should be noted that this decrease of the magnetic shear means that the outer magnetic field has weaker magnetic shear, and it does not mean that the magnetic shear is reducing during a flare.

In this paper, we focus on the question of what changes occur when a flare goes from the impulsive phase to the main phase. What causes this change, and how? The magnetic shear may show abrupt changes during a flare as reported in the above papers. The question we address here is: could the change from the impulsive to gradual phase be related to the magnetic shear change? For example, does the transition from the impulsive phase to the gradual phase occur as the initial flare brightenings evolve out of the filament channel into the larger surrounding volume?

To answer this question, we have selected a particularly well-observed X17 solar flare on October 28, 2003, which shows obvious shear change via the evolution of the EUV footpoints observed by TRACE, and examined the temporal evolution as well as the rate of change of the shear. The main observational data are summarized in Section 2. In Section 3.1 we present the comparison of EUV and HXR emission, and in Section 3.2 we study the pre-HXR EUV brightenings. The identification of the conjugate footpoints is described in Section 4.1. In Section 4.2 we focus on describing the decrease of the shear of the EUV footpoints, which is an apparent motion of the footpoints during the flare. The EUV emission mechanism of the brightenings is discussed in Section 5.1. Our interpretation of the evolution of the shear of the EUV footpoints is discussed in detail in Section 5.2. Conclusions are given in Section 6.

2. Observations

An X17 (GOES soft X-ray class) two-ribbon solar flare occurred in NOAA active region 10486 on October 28, 2003 at ≈11:00 UT. The main observational data used in this investigation were obtained simultaneously by the TRACE (Handy *et al.*, 1999) and the anticoincidence system (ACS) of the SPI spectrometer on board the ESA INTEGRAL satellite (Attié *et al.*, 2003; Vedrenne *et al.*, 2003). In addition to this large event, a filament eruption was seen in EUV (TRACE) and in Hα images (Figure 4 in Schmieder *et al.*, 2006 and Figure 2 in Wang *et al.*, 2005) about 40 min before the X17 solar flare and following a soft X-ray/EUV event which occurred about 10 min earlier (≈9:50 – 10:10 UT). Even though this filament eruption and the large flare that we studied involved the same magnetic inversion line, it is not clear whether they were related to each other, because of the large time difference. In this paper, we focus only on the X17 event.

During this event, SPI was observing the IC443 supernova remnant. Technical constraints fixed the satellite altitude in such a way that solar photons arrived at 122° from the telescope axis. At this incidence angle, the photons have to cross the satellite platform and the ACS of SPI. While the satellite platform practically is

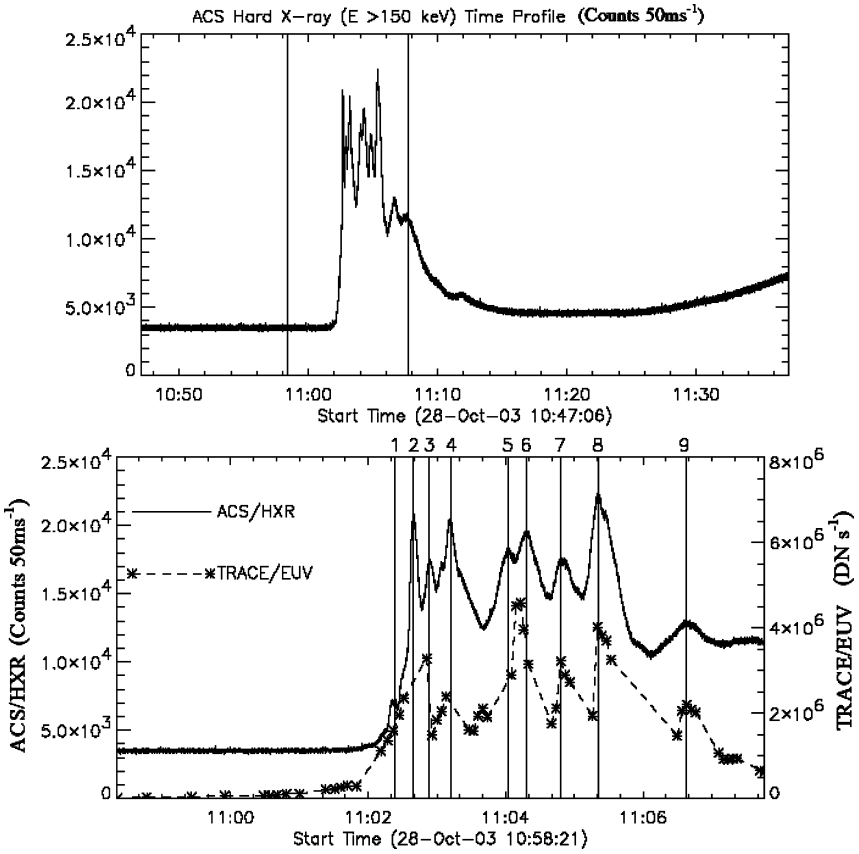

Figure 1. Light curves of the EUV and HXR emission. The SPI/ACS HXR light curve of the solar flare on October 28, 2003 is displayed in the *top panel*; the two lines mark the time range of the enlarged HXR light curve in the *bottom panel*, and nine spikes are marked by nine *vertical lines*. The summed TRACE/EUV light curve from all the brightenings is displayed via the *dashed line* with *asterisk signs* in the *bottom panel*.

transparent to the photons at such energies, the SPI/ACS system, composed of 5 cm thick BGO blocks, provides efficient shielding to photons arriving at the Germanium camera. On the other hand, the cross-section of this SPI/ACS, viewed under this 122° incidence angle, is ≈5200 cm^2. With a ≈100% efficiency from 150 keV up to some hundreds of keV, SPI/ACS is a very efficient detector for solar HXR in this energy range. As a result, count rates with 50 ms integration have been recorded with significant statistics, allowing a comparison of EUV and HXR intensity time profiles with very high precision. The SPI/ACS time profile of photons with energy $E > 150$ keV, in steps of 50 ms, is displayed in Figure 1. During the time period that we are interested in (bottom panel in Figure 1), nine peaks are seen and shown by the vertical lines. Peak 1, and Peaks 2 – 9 occurred during the rise phase and impulsive phase of the flare, respectively.

Given the high intensity of the flare, the number of photons detected in the SPI Ge detector matrix was sufficient to perform spectral analysis with 1 min integration time. The time profiles obtained for different energy bands suggest that during Peaks 1 – 4, photons with energies up to 10 MeV were emitted. The spectra integrated over these peaks show a clear power law bremsstrahlung spectrum (Gros *et al.*, 2004). Data from *Koronas*/SONG (Kuznetsov *et al.*, 2006) show that this spectrum extends up to 40 MeV. For the later peaks, it seems that this bremsstrahlung emission is mixed with nuclear (4 – 7 MeV) and pion (60 – 100 MeV) emissions.

TRACE observed AR 10486 from several hours before the flare until 12:56:46 UT on October 28, 2003, yielding data at 195 Å (Fe XII/XXIV), 284 Å (Fe XV), and 1600 Å (C IV plus UV continuum). Details of the TRACE instrumentation and performance can be found in Handy *et al.* (1999) and Golub *et al.* (1999). Observations at 195 Å and 1600 Å were recorded using an array size of 768×768 pixels, with a pixel size of 0.5 arcsecond, while the 284 Å observations used a 2×2 summed array of 512×512 pixels. Apart from the few 284 Å images taken, the observing mode was designed to alternate data acquisition between 195 Å and 1600 Å, with the time cadence at 195 Å higher than that at 1600 Å. To compare with HXR spikes, the TRACE data with high time cadence (typically $\approx$4 s) from 10:58:21 UT to 11:07:46 UT at 195 Å was selected. Due to the motion of the field of view (FOV), a small part of the north ribbon was sometimes not observed at 195 Å , but the ribbons in their entirety could be seen at 1600 Å and 284 Å at all times. TRACE observations show us that in the UV and EUV, the two flare ribbons are composed of discrete bright kernels (e.g., Figures 2 – 8). Our analysis focuses primarily on the observed evolution of these kernels during the course of the flare.

We note that some pixels in some of the EUV bright kernels saturated the Analog-to-Digital Converter (ADC) during the impulsive phase. We investigated the degree of saturation in the EUV images of this flare and found that (1) very few pixels (3%) saturated the ADC even for the brightest flare kernel, (2) the CCD itself did not reach saturation level (full well is five times greater than the ADC conversion limit), and (3) the saturated pixels were only slightly stronger than the other pixels in the kernels, as determined from analysis of the first-order images. This saturation will have some effect on the accuracy of the actual intensity of the flare kernel, but produces a negligible change in the shape of the summed light curves. Details of the method for investigating these effects are presented by Lin, Nightingale, and Tarbell (2001).

3. Comparison of EUV and HXR Emission

3.1. Correlation between EUV and HXR emission

The SPI/ACS HXR data have excellent temporal resolution, but essentially no spatial resolution, while the TRACE data have both temporal and spatial resolution.

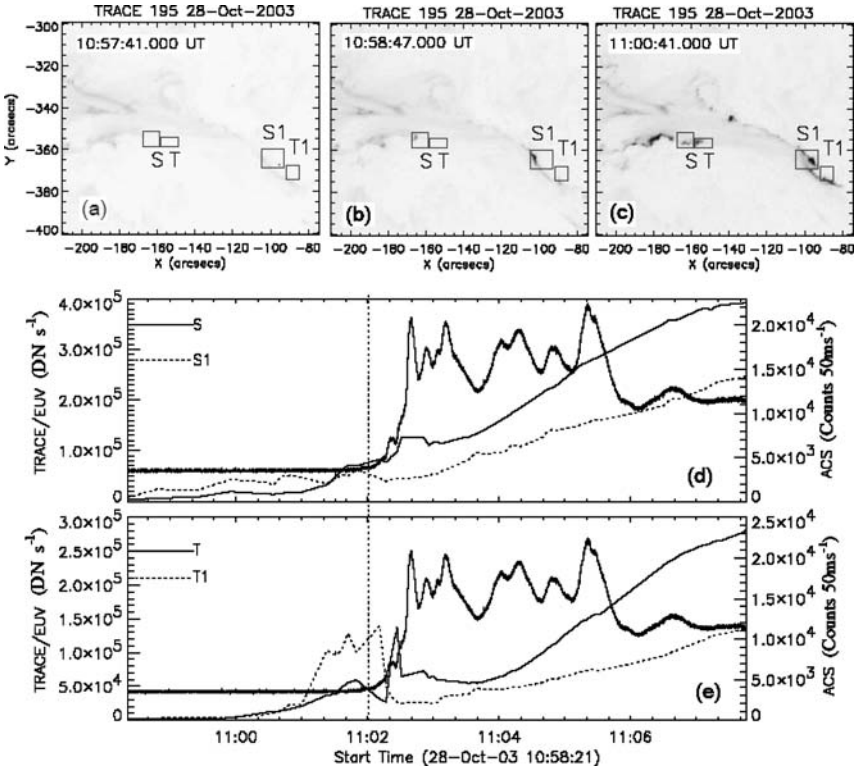

Figure 2. SPI/ACS/HXR light curves, TRACE/EUV images, and light curves of different brightenings during Phase 1. Phase 1 is the time period before HXR onset, which is represented by the vertical *dashed line*. (a) *Gray boxes* representing EUV brightenings "S"/"S1" and "T"/"T1" during Phase 1 are overlaid on an EUV image before Phase 1. (b), (c) EUV images are overlaid with gray boxes representing the EUV brightenings during Phase 1. (d), (e) EUV light curves of the two pairs of brightenings "S"/"S1" and "T"/"T1" during Phase 1. The ACS/HXR light curve is represented by the *thick solid line*.

RHESSI was behind the Earth at the start of this flare and began observations at 11:06:26 UT, which only caught the last HXR peak (Peak 9) in the impulsive phase. Our basic method of comparison to determine whether the EUV and HXR emissions are correlated is therefore based mainly on the timing of the EUV brightenings *versus* the timing of the HXR peaks.

In order to compare the EUV emission from the bright kernels and the HXR emission, boxes are defined in the EUV images that enclose the bright kernels. Because the bright kernels are continuously evolving (*viz.*, Fletcher, Pollock, and Potts, 2004), in order to track them we divide the rising and impulsive phases of this flare into eight time bins. Different boxes are chosen at the different time bins (see Figures 2 – 8) and the relevant kernels located in the boxes are labelled A, B, etc.

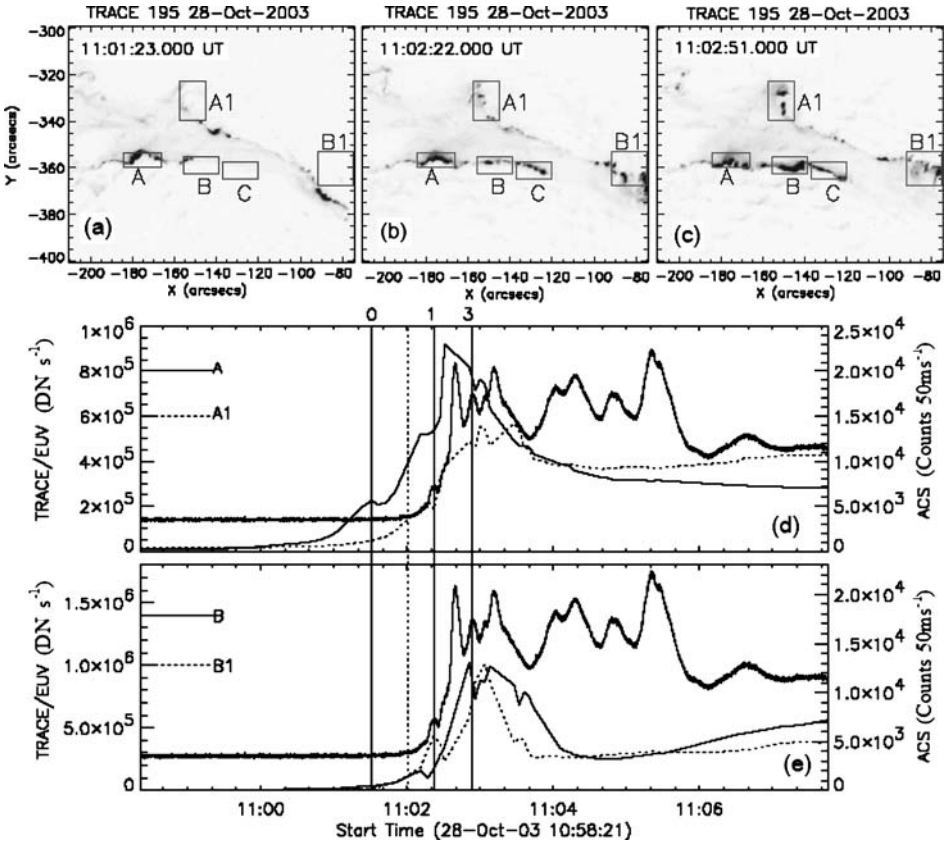

Figure 3. Similar to Figure 2 but for Phase 2. Phase 2 is the time period between the vertical *dashed line* representing HXR onset and the *solid line* representing Peak 3. (a) EUV image at EUV peak 0 before HXR onset is overlaid with *gray boxes* representing the EUV brightenings "A"/"A1," "B"/"B1," and "C" during Phase 2. (b), (c) *Gray boxes* representing EUV brightenings during Phase 2 are overlaid on EUV images closest in time to HXR Peaks 1 and 3. (d), (e) Similar to Figures 2d and 2e, but for EUV brightenings "A"/"A1," "B"/"B1," and "C" during Phase 2. The peaks are marked as *vertical line*.

The bottom panel in Figure 1 shows us the comparison of the hard X-ray light curve and the summed light curve of all the EUV bright kernels (for example, during Phase 1 it is the summed light curve of brightenings "S"/"S1" and "T"/"T1"). We can obtain a timing comparison, which is better than the cadence of the individual TRACE images by cross-correlating this summed EUV light curve as a whole against the HXR light curve. From Figure 1 we can see that the correlation between the HXR and EUV emission is very good, especially for HXR Peaks 3, 4, 7, 8, and 9. In order to quantify the temporal relationship between the HXR and EUV emission, we have done a cross-correlation between these two emissions for the individual HXR Peaks 4, 7, 8, and 9, and also a correlation of the full light curves

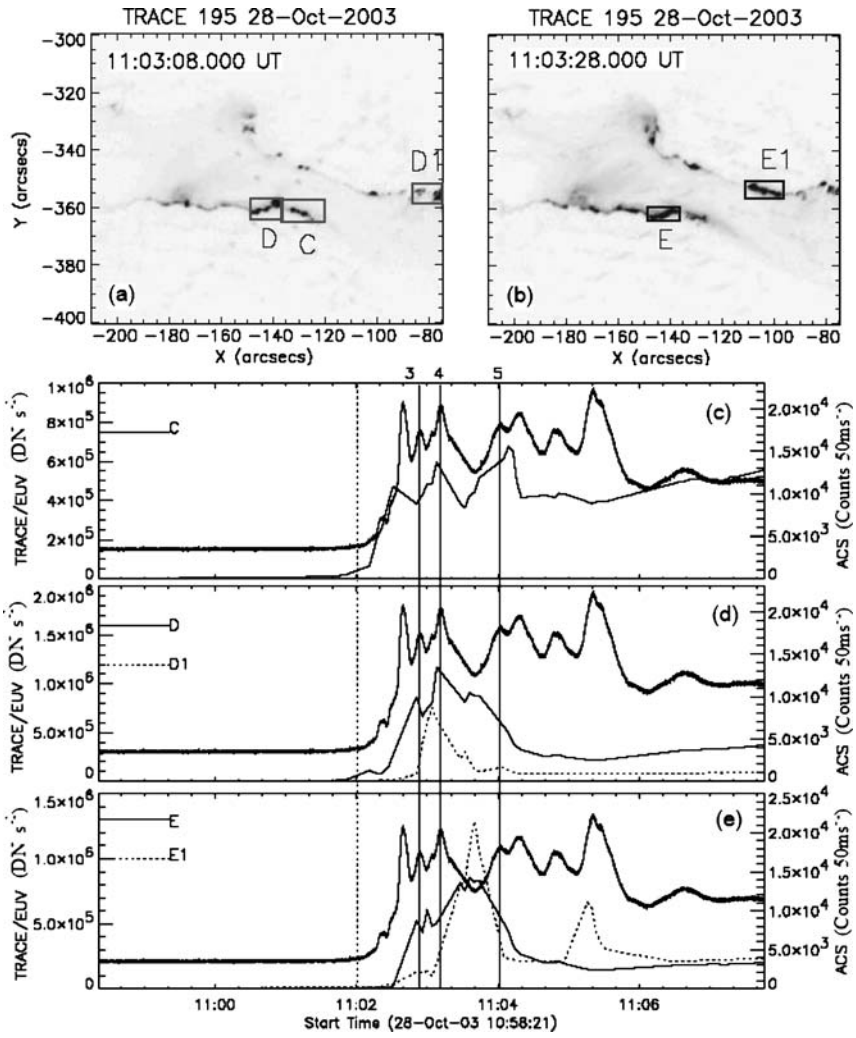

Figure 4. Similar to Figure 2, but for Phases 3 and 4. The time period between Peaks 3 and 4 is Phase 3, and Phase 4 is the time period between Peaks 4 and 5. (a) EUV image closest in time to HXR Peak 4 is overlaid with *gray boxes* representing the EUV bright kernels "C" and "D"/"D1" during Phase 3. (b) EUV image is overlaid with gray boxes representing the bright kernels E/E1 during Phase 4. (c), (d), and (e) Similar to Figures 2d and 2e, but for EUV brightenings during Phases 3 and 4, respectively.

from 10:58:21 UT to 11:07:46 UT. The time lags ($t_{\rm EUV} - t_{\rm HXR}$) obtained for the individual peaks are displayed in Table I, and the average time lag for these four peaks taken as an aggregate is 0.75 ± 1.4 s. The cross-correlation between the two complete light curves shown in the bottom panel in Figure 1 gives a time lag ($t_{\rm EUV} - t_{\rm HXR}$) of -1.25 ± 2.15 s (last line in Table I). From these results, we see that these

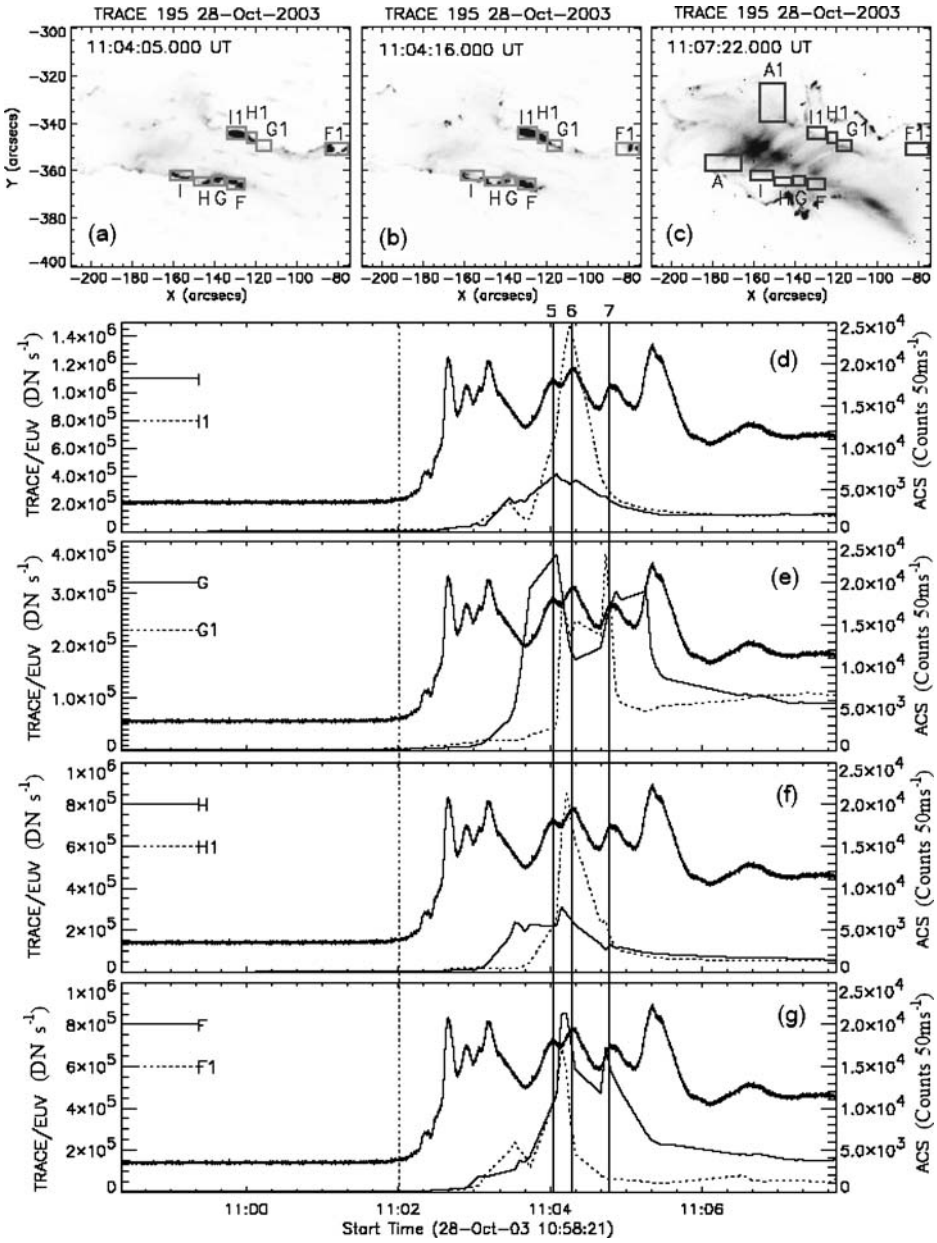

Figure 5. Similar to Figure 2, but for Phase 5 (the time period between Peaks 5 and 7). (a), (b) *Gray boxes* representing EUV brightenings during Phase 5 are overlaid on the EUV images closest in time to HXR Peaks 5 and 6, respectively. (c) *Gray boxes* representing EUV brightenings are overlaid on an EUV image of the postflare loops. (d), (e), (f), and (g) Similar to Figures 2d and 2e, but for EUV brightenings during Phase 5.

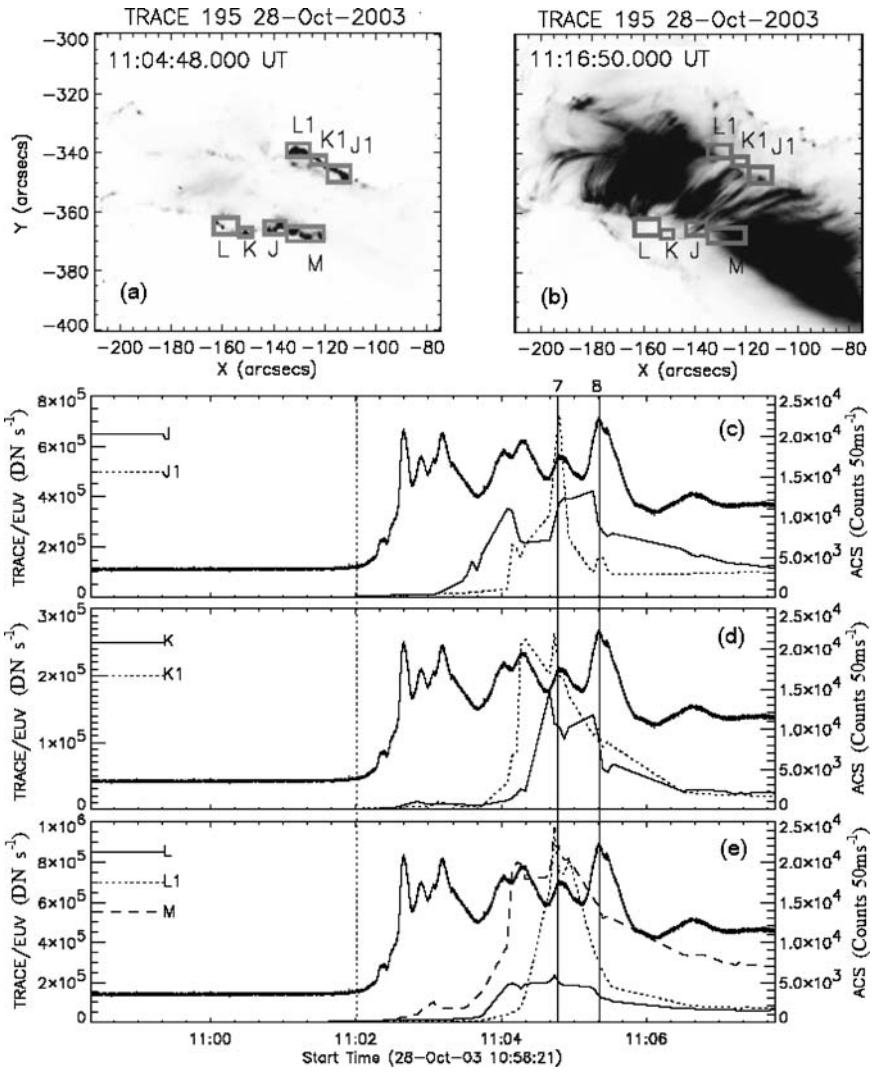

Figure 6. Similar to Figure 2, but for Phase 6 (the time period between Peaks 7 and 8). (a) *Gray boxes* representing EUV brightenings during Phase 6 are overlaid on the EUV image closest in time to HXR Peak 7. (b) *Gray boxes* representing EUV brightenings during Phase 6 are overlaid on an EUV image of the postflare loops. (c), (d), and (e) Similar to Figures 2d and 2e, but for EUV brightenings during Phase 6.

two types of emission are effectively simultaneous to our measurement accuracy, which is in the range $\approx 1-3$ s.

With the high spatial resolution of TRACE, we also examined the light curves of individual bright kernels (Figures 2 – 8) in order to find the EUV bright kernels corresponding to each HXR peak, and the resulting identifications are listed in

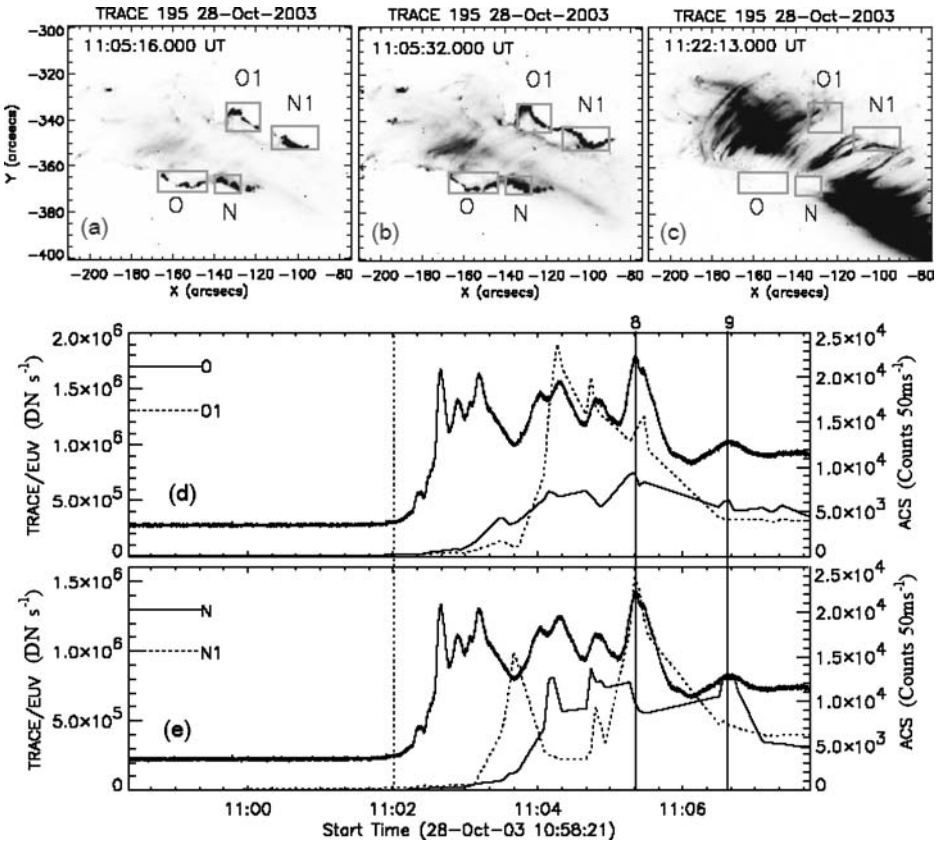

Figure 7. Similar to Figure 2, but for Phase 7 (the time period between Peaks 8 and 9). (a), (b) *Gray boxes* representing EUV brightenings during Phase 7 are overlaid on the EUV image closest in time to HXR Peak 8 and another EUV image during Phase 7, respectively. (c) *Gray boxes* representing EUV brightenings during Phase 7 are overlaid on an EUV image of the postflare loops.(d), (e) Similar to Figures 2d and 2e, but for EUV brightenings during Phase 7.

Table I. Table I presents the times of the HXR peaks, time lags between the EUV and HXR emission, and the EUV bright kernels corresponding to each HXR peak. The second column in Table I refers to the time of the HXR peak, and the third column shows the time of the EUV observations closest in time to each HXR peak. The fourth column shows the time lags between the HXR and EUV emission determined from a cross-correlation analysis of the respective peaks, and the error bar $(1 - \sigma)$ is given in the same column. The last column identifies the EUV bright kernels, which we believe are corresponding to the HXR peak. From Table I we can see that in the EUV observations closest in time to nearly each HXR peak, we find a peak in the EUV light curves from one or more bright kernels. These bright kernels are therefore possibly related to the HXR peak. We do not find the corresponding

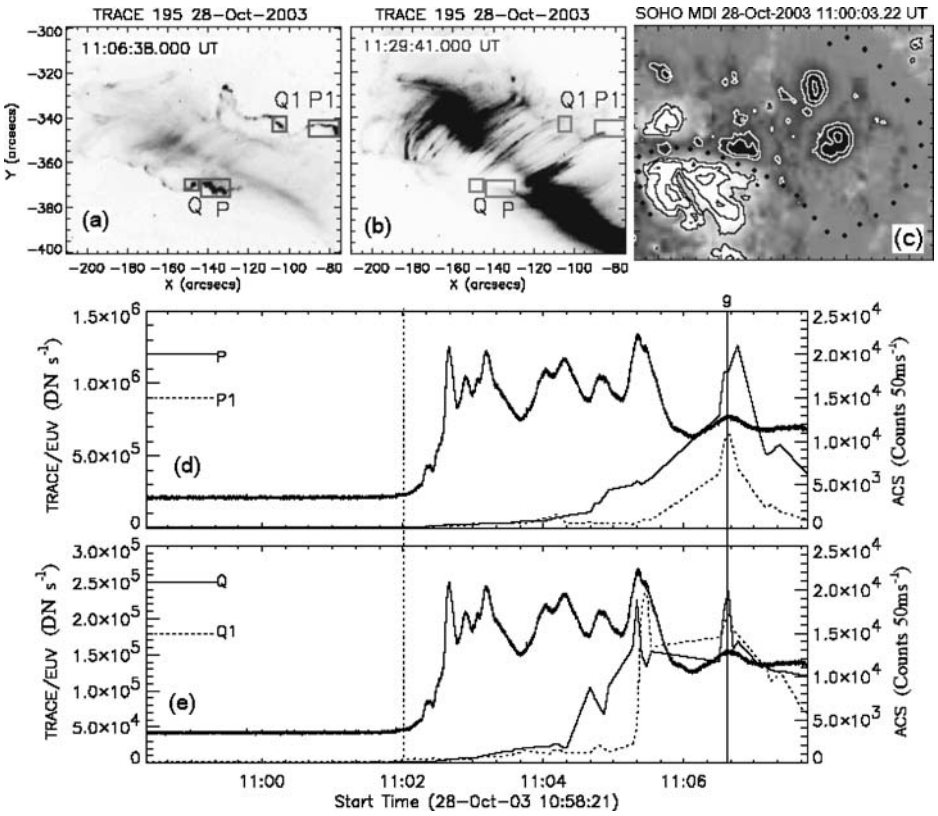

Figure 8. Similar to Figure 2, but for Phase 8 (the time period after Peak 9). (a) *Gray boxes* representing EUV brightenings during Phase 8 are overlaid on the EUV image closest in time to HXR Peak 9. (b) *Gray boxes* representing EUV brightenings during Phase 8 are overlaid on a later EUV image of the postflare loops. (c) SOHO/MDI photospheric magnetogram overlaid with MDI contours, where *white* and *black contours* refer to negative and positive magnetic field, respectively. The *black dotted line* represents the locus of the filament. The field of view is $240'' \times 160''$. (d), (e) Similar to Figures 2d and 2e, but for EUV brightenings during Phase 8.

EUV bright kernels for HXR Peak 2, but we note the lack of EUV observations near the time of that peak.

3.2. PRE-HXR EUV BRIGHTENINGS

From the light curves in Figures 1 and 2 we can see that the EUV emission from the bright kernels starts to rise at 10:58:21 UT, which is more than 3 min before the onset of the first HXR burst (11:02:00 UT). We also see some small peaks in the EUV light curves (e.g., Peak 0 in Figure 3d) before HXR onset.

EUV brightenings before the HXR onset appear within two slender ribbons, as can be seen in Figures 2b and 2c. The comparison of the morphology of the

TABLE I
Timing of HXR peaks and corresponding EUV brightenings.

Peak	SPI/ACS HXR ($E > 150$ keV) t_{HXR} (UT)	TRACE/EUV (195 Å) t_{EUV} (UT)	Time lag $\triangle t = t_{EUV} - t_{HXR}$ (s)		Corresponding TRACE/EUV Bright kernels
Peak 1	11:02:23.373	11:02:22			B1
Peak 2	11:02:39.573	11:02:31			
Peak 3	11:02:53.773	11:02:51			A1, B
Peak 4	11:03:11.923	11:03:08	−2.8	±1.2	C, D
Peak 5	11:04:02.323	11:04:05			I, G
Peak 6	11:04:18.423	11:04:13			I1
Peak 7	11:04:47.923	11:04:48	1.8	± 1.0	J1
Peak 8	11:05:20.823	11:05:20	2.9	± 1.0	O, N1
Peak 9	11:06:37.323	11:06:38	1.1	± 2.4	P1, Q/Q1
Total			−1.25	± 2.15	

pre-HXR brightenings and the later flare ones (*viz.*, Figure 3a) shows us that the flare brightenings result from an outward expansion of the pre-HXR EUV brightenings in a direction perpendicular to the ribbons and an extension of the pre-HXR brightenings along the direction of the ribbons (Figures 9a – e). Some of the flare brightenings are also seen before the HXR onset, such as brightening "A." These observations show that the preflare EUV brightenings are very similar to the flare ones, differing mainly in intensity but similar to the later flare brightenings in most other respects.

4. Evolution of the EUV Bright Kernels

4.1. Identification of the EUV conjugate footpoints

The most prominent conjugate footpoints have been identified manually by studying the evolution of the EUV bright kernels. There are three factors that we considered in identifying brightenings as conjugate footpoints: (1) the two brightenings appear simultaneously, (2) the light curves of the two brightenings are very similar, and (3) the two brightenings are connected by postflare loops. In this section we focus on describing in detail several examples of the method to show how we track and identify the conjugate footpoints in this flare.

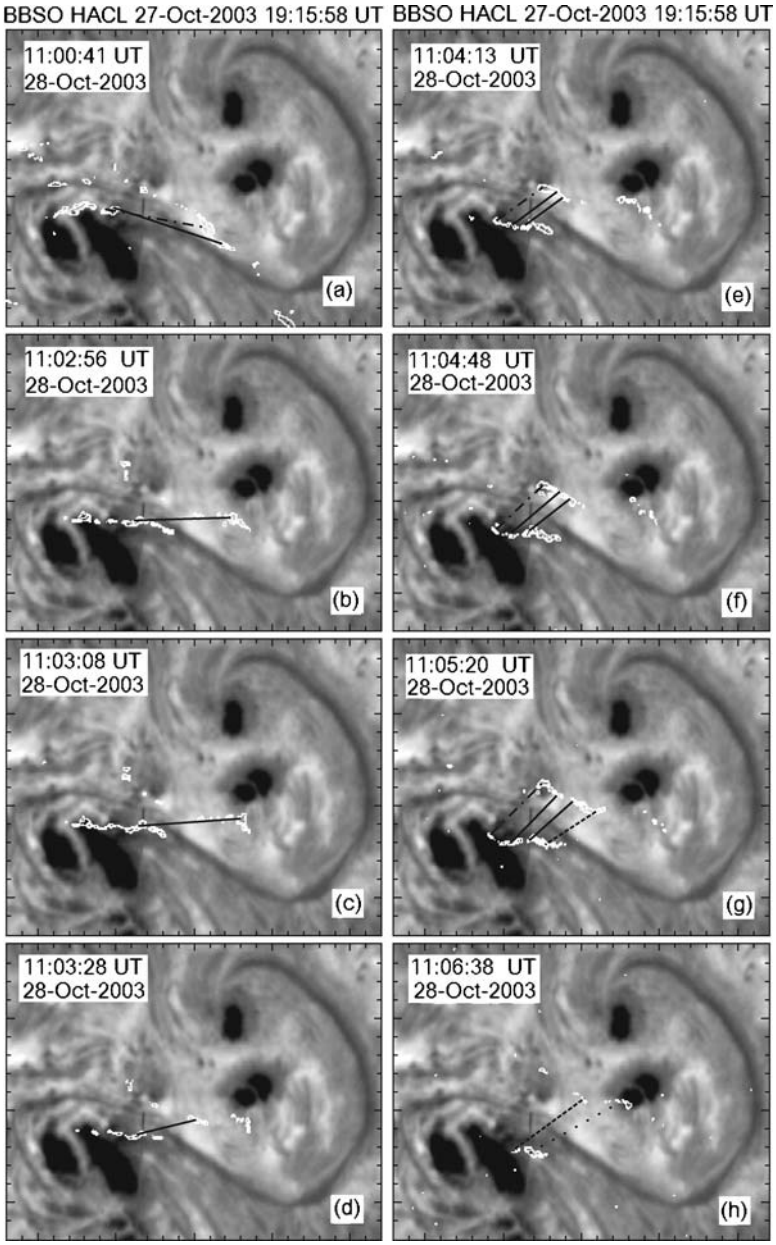

Figure 9. EUV brightenings and Hα image. TRACE/EUV contours at different times are overlaid on an earlier Hα image from BBSO. The times of the EUV contours are marked on each image, and the *black lines* connecting to the EUV bright kernels represent the possible conjugate EUV footpoints. Different kind of line refers to different group of brightening pairs. The field of view is $240'' \times 160''$ for each image.

Most of the EUV conjugate footpoints before Phase 5 have similar light curves, and some of the pairs can also be identified as appearing at the same time. These early brightenings are close to the neutral line and any possible postflare loops connecting them would be hidden under the larger postflare loops connecting the outer brightenings (see below for a discussion of the relative timing). Since no corresponding postflare loops can be seen, we identify the conjugate footpoints mainly by the first two factors.

For example, at 10:58:21 UT, the first EUV brightening "S1" appears in the western part of the north ribbon and spreads from east to west. The next brightening, "S," located in the eastern part of the south ribbon appears at 10:58:47 UT and spreads from east to west (Figure 2b). Because (i) only these two brightenings can be seen at this time, (ii) the time of their appearance is quite close, and (iii) the two light curves are also similar, we speculate that brightening "S" may be associated with brightening "S1."

With the extension of the two ribbons from east to west, brightenings "T" and "T1" appear at 11:00:41 UT (Figure 2c). Brightenings "T" and "T1" may be conjugate footpoints, because they appear at the same time and have similar time profiles during Phase 1 (Figure 2e).

After Phase 4, we identify the EUV conjugate footpoints mainly by factors (2) and (3), since many brightenings appear simultaneously, and postflare loops are seen for these kernels. Although the correlation between the light curves of some of these conjugate footpoints is not clear, they can be confirmed by the corresponding postflare loops. For example, many EUV brightening pairs appear at HXR Peak 5, but the conjugate nature of footpoints "I"/"I1," "H"/"H1," "G"/"G1," and "F"/"F1" may be confirmed from the appearance of postflare loops (Figure 5c) connecting them.

For some conjugate brightening pairs before 11:04:05 UT, we do not see the expected postflare loops, but this does not mean that they are not conjugate footpoints. Cargill, Mariska, and Antiochos (1995) derived a simple formula for the cooling time of high-temperature flare plasma, which is $\tau_{\rm cool} \approx 2.35 \times 10^{-2} L^{5/6} / T_0^{1/6} n_0^{1/6}$s. The parameters L, T_0, and n_0 in the formula are the loop half-length, electron temperature, and electron density, respectively. From the formula we can see that the most sensitive parameter is the loop length. The distance between the earlier brightening pairs before Phase 5 is much longer than that between the later brightening pairs (Figures 2 – 8). Because of their large separation along the neutral line, these early loops are two to three times longer than the later loops, so it should take substantially longer for the earlier loops to cool down to the TRACE/EUV observational temperature range than the later ones. By the time they cool down to the TRACE temperature range, the shielding by the overlying loops makes them unobservable.

Table II gives a summary of the brightenings occurring in the different phases of the flare. Note that the different phases in this table just refer to the different time bins and they do not have physical implication. The start and end times of the phases

TABLE II

Summary of the bright kernels occurring in different phases of the October 28, 2003 flare.

Phase	TRACE (195 Å) Brightening kernels						Ribbon	Angle θ (°)
Phase 1 (Figure 2)				T	S		S	
10:58:21 – 11:02:10				T1	S1		N	73, 71
Phase 2 (Figure 3)	C			B		A	S	
11:02:11 – 11:02:55				B1		A1	N	54
Phase 3 (Figure 4)	C			D			S	
11:02:56 – 11:03:27				D1			N	50
Phase 4 (Figure 4)				E			S	
11:03:28 – 11:04:04				E1			N	41
Phase 5 (Figure 5)	F		H	G	I			
11:04:05 – 11:04:47	F1		H1	G1	I1		N	18
Phase 6 (Figure 6)	M		K	J	L		S	
11:04:48 – 11:05:19			K1	J1	L1		N	19
Phase 7 (Figure 7)		N		O			S	
11:05:20 – 11:06:29		N1		O1			N	9, 23
Phase 8 (Figure 8)	P	Q					S	
11:06:30 – 11:07:46	P1	Q1					N	20

are displayed in the first column. The middle columns give the identifying labels of the different bright kernels in each ribbon. The grouping of the identifying letters into different vertical columns (e.g., "T"/"T1," "B"/"B1," "D"/"D1," "E"/"E1") indicates the evolution of a pair of conjugate footpoints through the stages of its evolution. The middle column marked between the two vertical lines represents the strongest brightening pairs, and the positions of these brightening pairs appear to evolve continuously during the evolution of the flare (especially for the brightenings in the south ribbon). The next column indicates which ribbon (North (N) or South (S)) the bright kernels occurred in. These identifications are then used to define an angle θ, listed in the last column and discussed in the next section.

4.2. Evolution of the shear of the EUV conjugate footpoints

It is well known that filaments typically lie on inversion lines in the longitudinal magnetic field when viewed near the center of the disk (McIntosh, 1972), which also can be seen in Figure 8c. In order to get information about the ribbon's underlying magnetic inversion line, we use the solar filament which can be seen in Hα

image obtained at Big Bear Solar Observatory (BBSO). Because there are no Hα observations at BBSO close in time to the preflare phase, we choose an image late in the day on October 27, 2003, which is about 15 h before this flare.

To get good coalignment of the TRACE/EUV and BBSO/Hα images, we proceeded in three steps: (i) we derotated the Hα image to the same time as the EUV image, and found the SOHO/MDI magnetogram closest in time to the EUV image; (ii) we overlaid the Hα image with the SOHO/MDI magnetogram, using the dark sunspots; (iii) we selected the two images in 195 Å closest in time from SOHO/EIT and TRACE/EUV, and obtained the offset of the TRACE/EUV image by cross-correlation.

In order to examine the evolution of the shear of the EUV conjugate footpoints, we select one image from each time bin; the EUV contours in the different time bins overlaid on the Hα image can be seen in Figures 9a – g, and the conjugate footpoints obtained from our analysis are marked as black lines connecting the bright kernels. The different group of brightening pairs shown in Table II are indicated by different line types in the figure. The evolution of the shear is clearly seen in this sequence of images.

In order to calculate a shear angle, the conjugate brightening pairs during each of the phases connected by the solid, dot-dashed, and dashed lines as shown in the middle column marked between the two vertical lines in Table II are regarded as a group and the angles are averaged. The angles (shear angle) between the lines connecting these conjugate footpoints and the line perpendicular to the filament have been measured and displayed in the last column in Table II. The angles between the lines connected different brightenings pairs in this group are very similar at each phase (time bin) during the early phases (time bins), but become more dispersed after Phase 6. For example, the angle between the line connecting brightening pair "N"/"N1" and the line perpendicular to the filament is very different (23° vs. 9°) from the angles measured for the other brightening pairs seen in Phase 7. All values, however, are retained when taking the average.

Because most of the strongest brightening pairs predominating at the earlier phases (time bins) disappeared by Phase 8, the angle θ is measured using brightening pair "Q"/"Q1," which appears to be related to the brightening pair "N"/"N1" in position. Because the brightening pairs which are associated with the strongest brightening pair "P"/"P1" at Phase 8 are outside of the FOV most of the time, the evolution of this group of brightening pairs is not discussed here.

Furthermore, we have also examined the rate of change of these angles ($-d\theta/dt$; we use the average value of θ, if we have more than one value in a given time bin), which is shown in the first column in Table III, and the corresponding time (we use the midpoint between the two times at which we measured the two angles) is displayed in the second column.

The ACS/HXR time profile is displayed in Figure 10a. The temporal evolution of the average shear angle θ and the change rate of this angle $d\theta/dt$ are displayed as a solid line with asterisk signs and a dashed line with plus signs, respectively in

TABLE III
Shear angle change rate and the corresponding time.

Time (UT)	11:01:48	11:03:02	11:03:18	11:03:48	11:04:30	11:05:04	11:05:59
$d\theta/dT(^{\circ}s^{-1})$	0.14	0.33	0.45	0.51	0.03	0.03	−0.07

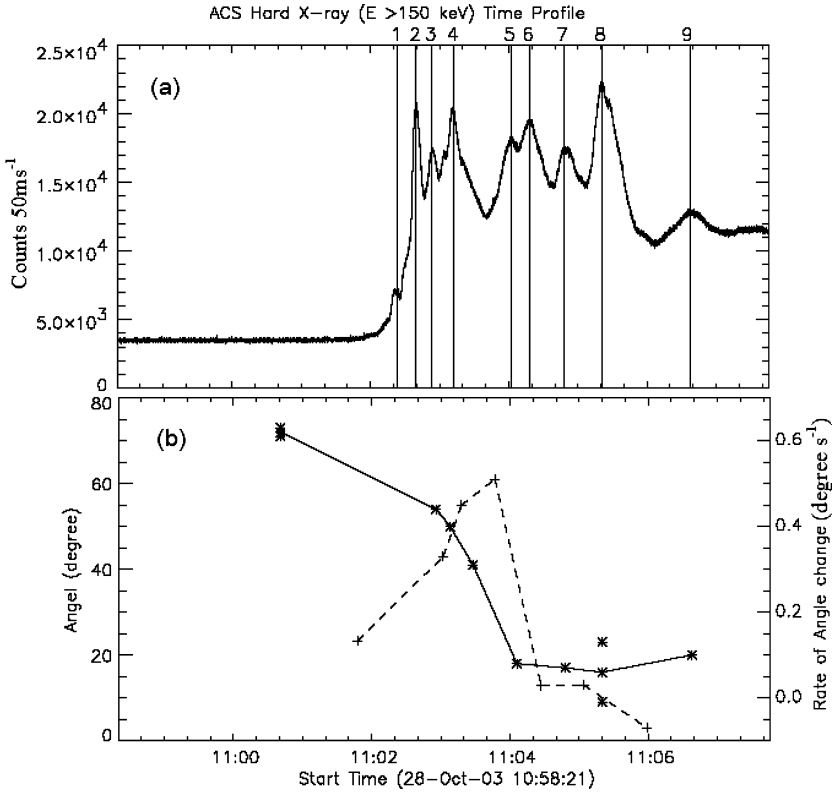

Figure 10. HXR light curve and the temporal evolution of the shear angle and the change rate of this angle. (a) The ACS/HXR light curve of the solar flare on October 28, 2003. (b) The evolution of the shear angle θ (*solid line* with *asterisk sign*), and the evolution of the change rate of this angle (*dashed line* with *plus sign*).

Figure 10b. The real measured angles are shown as individual asterisk signs around the average angle.

From Figure 10b we see that the shear angle θ of the strongest brightening pairs is decreasing all the time during the early impulsive phase, which indicates that the shear of the conjugate footpoints is decreasing during the early impulsive phase (before Peak 6). The change rate of the shear angle peaks during the early impulsive phase, as can be seen in Figure 10b, and the shear change becomes very slow after

Peak 5. It seems, therefore, that the change in shear angle of the EUV brightenings does not correlate in a straightforward way with the impulsive-phase HXR bursts.

5. Discussion

5.1. EUV BRIGHTENINGS GENERATION MECHANISM

As mentioned previously, there are mainly two generation mechanisms for the EUV brightenings: thermal conduction from the reconnected loops, and direct bombardment of the lower atmosphere by accelerated particles from the reconnection site. By the comparison of the EUV and HXR emission, we are able to discuss the EUV brightenings generation mechanism in this event.

Thermal conduction models have been proposed where the initial instability occurs at the loop top where the gas is heated and produces hard X-rays. A thermal conduction front proceeds down the loop to heat the chromosphere to at least transition region temperatures (Smith and Lilliequist, 1979; Smith and Auer, 1980; Nagai, 1980).

TRACE/EUV image overlaid with RHESSI HXR ($E = 100 - 200$ keV) image at the time period of the HXR Spike 9 has been shown in Figure 9 in Krucker and Hudson (2004). From that figure, we can see the HXR sources are located within the two EUV ribbons rather than at the loop top, and we also can see the strongest HXR sources are corresponding to the strongest EUV brightening pair "P"/"P1." These observations suggest that the EUV brightenings during HXR Spike 9 may not be due to thermal conduction.

Unfortunately, we do not have HXR image before HXR spike 9 to check the viability of the thermal conduction model for the other EUV brightenings. However, the travelling time of the thermal conduction front can be estimated as $t = L^2 n_e k_B / \kappa_0 T^{5/2}$ (Yokoyama and Shibata, 1997), where k_B is Boltzmann constant, κ_0 is a physical constant (about 10^{-6} in cgs). Here, L, n_e, and T are the half length of the loop, electron number density, and the temperature of the hot plasma, respectively. Our event is located close to disk center, so we cannot measure the length of the loops directly because of the viewing angle. However, we can measure the distance between the EUV conjugate footpoints. The shortest distance between the EUV conjugate footpoints for Peaks 4, 7, 8, and 9 is approximately 28 800 km, thus the half-length of the shortest loop should be approximately 23 000 km, if we assume a semicircular loop. If we assume that the electron number density and the temperature of the hot plasma are 2×10^{9} cm^{-3} and 20 MK, respectively, the travelling time will be 0.94 s, which is comparable to the observed time delay (less than 3 s) between the EUV and HXR emission. This means that we cannot rule out thermal conduction as the cause of the EUV brightenings. However, we should note that the temperature is the most sensitive parameter in this equation: the higher the temperature is, the shorter the travelling time is. The temperature that we used

above is within the range of Fe XXIV emission, which starts to appear after Peak 9, as can be seen in Figure 5c, so this travelling time may be only appropriate for the later brightenings after Peak 9. However, due to the lack of HXR observations with spatial resolution, we cannot rule out the possibility that the HXR emission is from a hot ($T > 20$ MK) loop-top source; therefore, we cannot rule out the possibility of the thermal conduction.

As mentioned in Section 3.2, the observations show that the preflare EUV brightenings are similar to the later flare ones in most respects, differing mainly in intensity. Therefore, we speculate that the pre-HXR EUV brightenings have the same generation mechanism as the flare ones. Why can we see EUV brightenings before the HXR onset in this event? The EUV observations show that the pre-HXR EUV bursts are much weaker than the later ones, as can be seen from the summed EUV light curves in the bottom panel of Figure 1. Given the high count rates and good statistics seen in the HXR for all of the flare peaks, the HXR sensitivity does not seem to be an issue. We therefore suggest that the energy released from the reconnection site may be relatively low during the rising phase, so that there is less contribution to the HXR emission in the SPI/ACS energy band ($E > 150$ keV).

5.2. Evolution of the magnetic shear

The EUV bright kernels are argued to represent the chromospheric footpoints of the newly reconnected flare loops. Therefore, we can to some extent infer the magnetic field connectivity by observation of the evolution of the EUV footpoints.

In order to study the shear change, the strongest brightening pairs of EUV footpoints, which represent the major energy release site are selected. A strong to weak shear change is observed during the impulsive phase, which confirms the earlier results found at other wavelengths (Masuda, Kosugi, and Hudson, 2001; Asai *et al.*, 2003; Kundu, Schmahl, and Garaimov, 2004). The decrease of the shear of the EUV footpoints implies that the newly reconnected loops have a lesser magnetic shear.

However, we also would like to know what these observations can tell us about the flare magnetic topology. The observed shear change can be understood in terms of the standard model for solar flares (e.g., Moore, LaRosa, and Orwig, 1995; Moore *et al.*, 2001). According to this model the preflare magnetic field contains a highly sheared core field overlying the magnetic inversion line (MIL) on the photosphere. It is assumed that the preflare configuration evolves appropriately for the sheared core field to become eruptively unstable, and that the flare begins with the onset of the core eruption. Magnetic field begins to reconnect just below the rising core field, producing newly reconnected loops that, though less sheared than the preflare core field, retain some obvious shear (see Figure 1 in Moore, LaRosa, and Orwig, 1995). This indicates that, soon after the start of the eruption, the reconnection site is located at some height above the photosphere, inside the sheared envelope field.

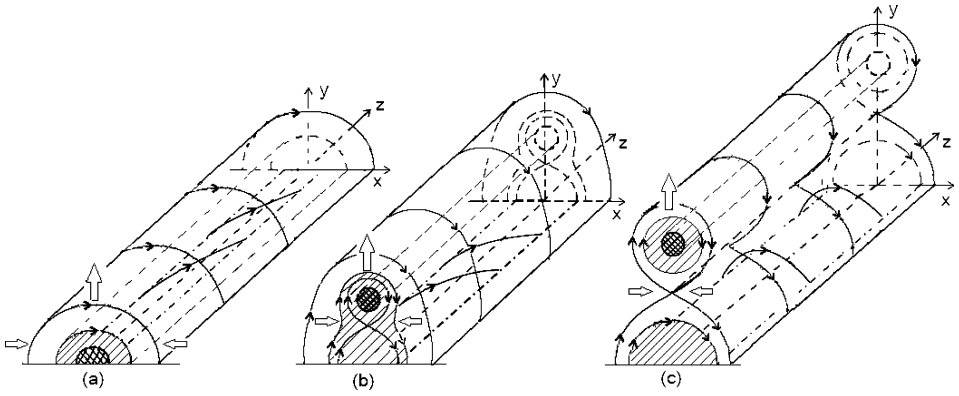

Figure 11. Cartoon of the evolution of the magnetic field in the standard model of solar flares. (a) Preflare magnetic field configuration with greatly sheared core field region (double hatched) surrounded by relatively less but still highly sheared envelope field (single hatched), which is underlying the unsheared envelope field. (b) Magnetic reconnection occurs in the highly sheared envelope field region. (c) The sheared envelope field splits completely, and magnetic reconnection occurs in the region where the field is unsheared. The direction of the magnetic field is represented by the *arrows* on the field lines. Note that the double-hatched shadings indicate magnetic shear, not the presence of cool plasma (Hα filament).

This reconnection causes the sheared envelope to split into two parts during the early phase of the flare. The upper part is ejected into the heliosphere, while the lower part stays behind on the sun.

Figure 11 illustrates the evolution of the magnetic field in the early phase of the flare according to the standard model, but focusing on the evolution of the shear of the magnetic field. We use a Cartesian coordinate system (x, y, z) with the origin lying on the MIL in the photosphere; x is the horizontal coordinate perpendicular to the MIL, y is the height above the photosphere ($y \geq 0$), and z is the distance along the MIL. Figure 11a shows the magnetic configuration well before the flare at a time when flare-related reconnection has not yet occurred. Figure 11b shows the configuration in the early phase of the flare when the main reconnection has already started. The transition from Figure 11a to Figure 11b may take 1 h or even longer. It is unclear exactly how this transition occurs. A detailed model of the magnetic field evolution during this period is beyond the scope of this paper.

It is useful to divide the initial magnetic field configuration into three parts: (1) the inner part is a bundle of greatly sheared core field (double hatched) located just above the MIL; (2) the envelope field immediately coating the sheared core bundle is relatively less but still highly sheared (single hatched); (3) the outmost part is unsheared magnetic field overlying the immediate sheared envelope (Figure 11a). Note that the shear of the magnetic field transitions gradually between these regions.

The observed high shear during the early impulsive phase indicates that magnetic reconnection occurred in the region where the magnetic field (highly sheared,

within the immediate sheared envelope region of Figure 11b) has a strong component along the direction of the magnetic inversion line. With the expansion of the sheared core flux bundle, the reconnection line moves upward, and the reconnection region moves out progressively. Therefore, the shear of the newly reconnected loops decreases progressively, which can explain the progressive decrease of the shear of the footpoints with the ribbon separation (Figures 9a – d).

The sheared envelope soon splits into two separate parts: an upper part that moves away from the sun and a lower part that stays behind in the low corona (Figure 11c). Magnetic reconnection occurs at an *X*-line located between the upper and lower parts of the sheared envelope field. As the eruption proceeds, the upper and lower parts of the sheared envelope field become more and more clearly separated, and the B_z component of magnetic field at the *X*-line decreases. Therefore, during the later phase, the newly reconnected loops are weakly sheared, as shown in Figure 11c. This model provides a natural explanation for the observed shear change.

At 11:04 UT, the shear angle is about 20°, and little change in shear angle occurs after that time (Figure 10). This suggests that the splitting of the sheared envelope field is nearly complete at 11:04 UT, in the middle of the impulsive phase. Hence, there is no obvious relationship between the splitting of the sheared envelope field and the end of the impulsive phase.

6. Conclusions

An X17 class (GOES soft X-ray) two-ribbon solar flare which occurred on October 28, 2003 is studied in this paper. Comparison of the light curves of the EUV emission from the brightenings within the two ribbons observed by TRACE and the HXR ($E > 150$ keV, SPI/ACS) emission show very good correlation, and we have also found that most of the individual peaks in the HXR bursts can be identified with EUV peaks from one or more bright kernels. The cross-correlation between the light curves of the two types of emission shows that the typical time delay between the EUV and HXR emission is less than 3 s in this event. The comparison of the HXR ($E = 100 – 200$ keV, RHESSI) and EUV image at Phase 8 shows that the HXR sources are located at the EUV bright points. Although all of these observations seem to be favorable to the explanation that the EUV brightenings are mainly caused by direct bombardment at the lower atmosphere of the energetic particles accelerated at the reconnection site, we cannot rule out the possibility of thermal conduction, since the travelling time of the thermal conduction front can be comparable to the observed time delay between the EUV and HXR emission, if the HXR emission is from a very high temperature ($T > 20$ MK) loop-top source. Good data sets observed simultaneously by TRACE, RHESSI, and the Solar-B/XRT, which will be launched in 2006 will be helpful in obtaining a more conclusive result in this topic.

The onset of the EUV brightenings is about 3 min earlier than the HXR emission. These pre-HXR EUV brightenings appear to be associated with the flare ones in position, and these two kinds of brightenings do not have any obvious major difference. Some of the flare brightenings are also seen before the HXR onset, such as brightening "A." All of these observations may suggest that the pre-HXR EUV brightenings have the same generation mechanism as the flare ones.

The EUV conjugate footpoints start at a position close to the magnetic inversion line but widely separated along the inversion line (highly sheared), and change into far from and straight across the inversion line (less sheared) gradually during the impulsive phase. This evolution of the EUV footpoints from strong to weak shear confirms the earlier results reported at other wavelengthes. This suggests that the observed evolution in shear during the initial stages of a flare may be a frequent occurrence. We propose an interpretation in terms of the splitting of the sheared envelope field of the greatly sheared core rope overlying the magnetic inversion line during the early phase of the event. It is clear now, there must be some sheared field left behind on the sun, but what is the fraction of this kind of sheared field, or how much sheared filed has been erupted? A lot of work needs to be done in order to answer this question.

Our most significant new result is that the shear (between the strongest EUV footpoints) change was very fast during the early impulsive phase, but stopped in the middle of the impulsive phase. This result may indicate that the sheared envelope field is split completely in the middle of the impulsive phase. This observation also gives a negative answer to our initial question: the magnetic shear change *per se* does not seem to be the reason for the transition from the impulsive phase to the main phase. More detailed studies of magnetic reconnection and particle acceleration in flares are needed in order to answer this question.

Acknowledgements

The authors thank the anonymous referee for the constructive suggestions to improve the level of this paper. The authors sincerely thank Dr. Spiro Antiochos, Dr. Jun Lin, and Dr. Guangli Huang for helpful discussions. Y.N. Su is grateful to Dr. Ed DeLuca, Dr. Mark Weber, and Dr. Jonathan Cirtain for their help with data reduction, and she also would like to thank Dr. Brigitte Schmieder, Dr. Arek Berlicki, and Dr. Pascal Démoulin for useful discussions and their hospitality during her stay in Meudon. Y. N. Su is also grateful to Dr. Jiong Qiu and Dr. Haisheng Ji for their help with BBSO data process. The authors wish to thank the team of TRACE, SPI/ACS, SOHO/MDI, SOHO/EIT, and NJIT/BBSO for providing the valuable data, and especially thank Dr. Andrei Bykov for letting them use his private SPI/ACS data. The TRACE analysis was supported at Smithsonian Astrophysics Observatory (SAO) by a contract from Lockheed Martin. Y.N. Su was also supported by SAO Predoctoral Fellowship and the NSFC projects No. 10333030 and 10273025.

References

Asai, A., Ishii, T.T., Kurokawa, H., Yokoyama, T., and Shimojo, M.: 2003, *Astrophys. J.* **586**, 624.

Attié, D., Cordier, B., Gros, M., Laurent, Ph., Schanne, S., Tauzin, G. *et al*.: 2003, *Astron. Astrophys.* **411**, L71.

Cargill, P.J., Mariska, J.T., and Antiochos, S.P.: 1995, *Astrophys. J.* **439**, 1034.

Carmichael, H.: 1964, in W.N. Hess (ed.), *NASA Symposium on The Physics of Solar Flares, NASA SP-50*, NASA, Washington, p. 451.

Cheng, C.-C., Tandberg-Hanssen, E., Bruner, E.C., Orwig, L., Frost, K.J., Kenny, P.J., Woodgate, B.E., Shine, R.A.: 1981, *Astrophys. J.* **248**, L39.

Cheng, C.-C., Tandberg-Hanssen, E., and Orwig, L.E.: 1984, *Astrophys. J.* **278**, 853.

Fletcher, L.: 2002, in A. Wilson (ed.), Solar Variability: *From Core to Outer Frontiers, ESA SP-506*, ESA Publications Division, Noordwijk, The Netherland, p. 223.

Fletcher, L. and Hudson, H.: 2001, *Solar Phys.* **204**, 69.

Fletcher, L., Pollock, J.A., and Potts, H.E.: 2004, *Solar Phys.* **222**, 279.

Golub, L., Bookbinder, J., DeLuca, E., Karovska, M., Warren, H., Schrijver, C.J., Shine, R., Tarbell, T., Title, A., Wolfson, J., Handy, B., and Kankelborg, C.: 1999, *Phys. Plasmas* **6**, 2205.

Gros, M., Tatischeff, V., Kiener, J., Cordier, B., Chapuis, C., Weidenspointner, G., Vedrenne, G., von Kienlin, A., Diehl, R., Bykov, A., Méndez, M.: 2004, in V. Schönfelder, G. Lichti, and C. Winkler (eds.), *Proceedings of the 5th INTEGRAL Workshop on the INTEGRAL Universe, ESA SP-552*, ESA Publications Division, Noordwijk, The Netherland, p. 669.

Handy, B.N., Acton, L.W., Kankelborg, C.C., Wolfson, C.J., Akin, D.J., Bruner, M.E. *et al*.: 1999, *Solar Phys.* **187**, 229.

Hirayama, T.: 1974, *Solar Phys.* **34**, 323.

Huang, G.L. and Ji, H.: 2005, *Solar Phys.* **229**, 227.

Ji, H., Wang, H., Goode, P.R., Jiang, Y., and Yurchyshyn, V.: 2004a, *Astrophys. J.* **607**, L55.

Ji, H., Wang, H., Schmahl, E.J., Qiu, J., and Zhang, Y.: 2004b, *Astrophys. J.* **605**, 938.

Kane, S.R., Frost, K.J., and Donnelly, R.F.: 1979, *Astrophys. J.* **234**, 669.

Kopp, R.A. and Pneuman, G.W.: 1976, *Solar Phys.* **50**, 85.

Krucker, S. and Hudson, H.S.: 2004, in R.W. Walsh, J. Ireland, D. Danesy, and B. Fleck (eds.), *Proceedings of the SOHO 15 Workshop, ESA SP-575*, ESA Publications Division, Noordwijk, The Netherland, p. 247.

Kundu, M.R., Schmahl, E.J., and Garaimmov, V.I.: 2004, in A.V. Stepanov, E.E. Benevolenskaya, and A.G. Kosovichev (eds.), *Multi-Wavelength Investigations of Solar Activity, IAU Symp.* **223**, Cambridge University Press, Cambridge; New York p. 425.

Kuznetsov, S.N., Kurt, V.G., Yushkov, B.Y., Myagkova, I.N., and Kudela, K.: 2006, *Solar System Research* **40**, 104.

Lin, A.C., Nightingale, R.W., and Tarbell, T.: 2001, *Solar Phys.* **198**, 385.

Masuda, S., Kosugi, T., and Hudson, H.S.: 2001, *Solar Phys.* **204**, 57.

McIntosh, P.S.: 1972, in P.S. McIntosh and M. Dryer (eds.), *Solar Activity Observations and Predictions*, MIT press, Cambridge, Massachusetts, p. 65.

Moore, R.L., LaRosa, T.N., and Orwig, L.E.: 1995, *Astrophys. J.* **438**, 935.

Moore, R.L., Sterling, A.C., Hudson, H.S., and Lemen, J.R.: 2001, *Astrophys. J.* **552**, 833.

Nagai, F.: 1980, *Solar Phys.* **68**, 351.

Schmieder, B., Mandrini, C.H., Démoulin, P., Pariat, E., Berlicki, A., and Deluca, E.: 2006, *Adv. Space Res.* **37**, 1313.

Smith, D.F. and Auer, L.H.: 1980, *Astrophys. J.* **238**, 1126.

Smith, D.F. and Lilliequist, C.G.: 1979, *Astrophys. J.* **232**, 582.

Sturrock, P.A.: 1966, *Nature* **211**, 695.

Svestka, Z.: 1992, in Z. Svestka, B.V. Jackson, and M.E. Machado (eds.), *Eruptive Solar Flares*, Springer-Verlag, New York, p. 1.
Vedrenne, G., Roques, J.-P., Schönfelder, V., Mandrou, P., Lichti, G.G., von Kienlin, A. *et al.*: 2003, *Astron. Astrophys.* **411**, L63.
Wang, Y.M., Ye, P.Z., Zhou, G.P., Wang, S.J., Wang, S., Yan, Y.H., and Wang, J.X.: 2005, *Solar Phys.* **226**, 337.
Warren, H.P. and Warshall, A.D.: 2001, *Astrophys. J.* **560**, L87.
Woodgate, B.E., Shine, R.A., Poland, A.I., and Orwig, L.E.: 1983, *Astrophys. J.* **265**, 530.
Yokoyama, T. and Shibata, K.: 1997, *Astrophys. J.* **474**, L61.